PHYSICAL REVIEW B **81**, 195102 (2010)

Second harmonic generation in metamaterials based on homogeneous centrosymmetric nanowires

C. G. Biris* and N. C. Panoiu

Photonics Group, Department of Electronic and Electrical Engineering, University College London, Torrington Place, London WC1E 7JE, United Kingdom

(Received 4 February 2010; revised manuscript received 9 April 2010; published 4 May 2010)

We present a comprehensive theoretical study of the second harmonic generation (SHG) in metamaterials consisting of arbitrary distributions of cylindrical nanowires made of centrosymmetric materials. The electromagnetic field at both the fundamental frequency (FF) and second harmonic (SH), as well as the total cross section, the absorption cross section, and the scattering cross section, are calculated by means of a numerical algorithm based on the multiple scattering method. Our algorithm fully describes the nonlinear optical response of the metamaterial by incorporating the contributions of both the surface and bulk nonlinear polarizations and can be applied to both *s*- and *p*-polarized incident waves. We use this numerical method to investigate the SHG in a series of particular cases of practical interest, namely, a single metallic cylinder, chains of metallic cylinders, and periodic and random distributions of such cylinders. In particular, we study the relation between the local field enhancement, via the excitation of surface plasmon-polariton modes, and the amount of energy absorbed or scattered in the far-field, at the FF and the SH.

DOI: 10.1103/PhysRevB.81.195102 PACS number(s): 73.20.Mf, 78.67.Pt, 78.68.+m, 42.65.Ky

I. INTRODUCTION

With the emergence in the recent years of the research area of metamaterials,[1–19] we have witnessed a dramatic change of our approach to research in the physical properties of electromagnetic materials. Thus, during the last few years, it has become increasingly apparent that the effective, macroscopic optical properties of two-dimensional (2D) and three-dimensional (3D) (meta)materials can be dramatically altered by structuring them at a scale comparable or smaller than the operating wavelength. To be more specific, unlike the case of naturally occurring materials, the primary building blocks of metamaterials are characterized by a broad set of material and geometrical parameters, and therefore present a significant potential for designing materials with new or improved functionalities. For example, by a proper design of the primary unit cell of metamaterials it has been possible to demonstrate theoretically and then fabricate new materials with remarkable properties, such as materials that are magnetically active at terahertz and optical frequencies,[1–4] 3D,[5–9] and 2D[10,11] materials with negative index of refraction, frequency-selective surfaces,[12] transformation-optics electromagnetic media,[13–15] or low-index of refraction materials.[16–19]

It has been demonstrated that the "photonic atoms," which are the primary building blocks of photonic metamaterials, can be designed so as not only to emulate linear physical properties of regular atoms, such as magnetic moment[1] or electric polarizability,[20] but also to possess nonlinear optical properties, such as second-order[21–23] and third-order[24,25] nonlinear optical response. Following this analogy between optical materials made of atoms and metamaterials consisting of macroscopic photonic atoms, it becomes apparent that gaining a comprehensive understanding of the linear and nonlinear optical properties of these macroscopic building blocks is a prerequisite to a successful development of a general theory of optical metamaterials. To this end, of a particular importance is the case of metamaterials based on metallic nanoparticles, since in this case the primary constituents of the metamaterial support localized electromagnetic excitations, the so-called surface plasmon-polariton (SPP) modes,[26,27] whose resonant excitation can strongly affect the optical response of the metamaterial. In particular, at the corresponding resonance frequencies the electromagnetic field is strongly enhanced, an effect that dramatically influences the linear and nonlinear optical response of the metamaterial.

One of the main consequences of the plasmon-induced resonant enhancement of the electromagnetic field is that strong nonlinear optical effects can be achieved at relatively small optical power. This effect of SPP-induced resonant enhancement of nonlinear optical interactions has been employed in a series of important applications, such as single-molecule detection via surface-enhanced Raman scattering (SERS),[28] nanoscale antennae,[29] optically active guiding nanostructures,[30–32] or metallic nanotips for near-field optical microscopy.[33,34] In particular, the strength of second-order nonlinear optical effects, one relevant such optical process being the second-harmonic generation (SHG), is proportional to $|E|^4$, and therefore an enhancement of $\sim 10-100$ of the local field at the fundamental frequency (FF), easily achievable by using metallic nanoparticles, leads to an increase of up to 10^8 of the intensity of the light generated at the second harmonic (SH).[35–37] It should therefore be clear that in order to achieve a comprehensive characterization of the SHG in metallodielectric structures one has to employ theoretical methods and/or numerical simulations that enable one to accurately determine the spatial distribution of the electromagnetic field at the FF.

Since most metals are centrosymmetric media, i.e., they are invariant to the inversion symmetry transformation, it is of particular interest to develop robust theoretical models that describe the generation of the SH upon the scattering of light from ensembles of nanoparticles made of centrosymmetric materials. Recently, significant progress toward this goal has been made, with some notable examples being the theory of SHG from spherical[38] and cylindrical[39] particles of low-index contrast centrosymmetric materials or, more generally, SHG from a metallic cylinder.[40] It should be noted that in the former case the theoretical approach is valid only within the Rayleigh-Gans-Debye approximation, i.e., it is assumed that the field at the FF is not perturbed during the scattering process, whereas the latter approach only applies to a single scatterer.

In this paper we present a numerical method based on the multiple scattering matrix (MSM) algorithm, which can rigorously describe the general case, namely, the SHG from a collection of cylinders with arbitrary electric permittivity, which are made of centrosymmetric materials. In addition, we use this numerical method to study the SHG in several cases of theoretical and practical interest, namely, an isolated cylinder, chains of coupled cylinders, and ordered and randomly distributed arrays of cylinders. Importantly, our theoretical approach enables one to account for the contribution to the SH field of both the surface and the bulk nonlinear polarizations. The paper is organized as follows. In the next section we present the physical model and the mathematical formalism employed to determine the electromagnetic field at the FF and SH. Then, in Sec. III, we introduce several physical quantities, namely, the total cross section, the absorption cross section, and the scattering cross section, which are instrumental in characterizing the linear and nonlinear wave scattering. Subsequently, in Sec. IV, we apply our numerical method to study the linear and nonlinear wave scattering from a set of centrosymmetric cylinders. In particular, we consider the wave scattering by one cylinder, scattering by one-dimensional (1D) chains of cylinders, and the general case of wave scattering by 2D ordered and random distributions of cylinders. In the last section of the paper, we summarize and discuss our main conclusions.

II. MATHEMATICAL FORMALISM AND NUMERICAL ALGORITHM

The numerical algorithm used in our analysis is based on a recently introduced numerical method that describes the SHG in photonic crystals made of noncentrosymmetric quadratically nonlinear optical materials.[41] In this case, the dominant nonlinear optical interaction is described by the second-order nonlinear bulk polarization. However, this dipole contribution to the nonlinear polarization vanishes in the case of centrosymmetric materials and therefore the numerical method introduced in Ref. 41 cannot be used in its original form to study the SHG in this important class of materials.

In the approach introduced in this paper the calculation of the scattered field at the SH is performed in two stages. First, by using a standard MSM algorithm the electromagnetic field at the FF is calculated, and this field is subsequently used to determine the nonlinear polarization at the SH. In a second stage, this nonlinear polarization, which plays the role of the source of the field at the SH, is used to calculate the spatial distribution of the scattered field at the SH. Note that this two-stage approach implies that no energy is transferred back from the SH to the FF and therefore the numerical method presented here is valid only within the so-called undepleted pump approximation, i.e., when the energy at the FF dissipates only through linear optical losses. Due to the reduced conversion efficiency of the SHG interaction and the small size of the nanostructures involved in the nonlinear scattering process, the undepleted pump approximation is valid in all cases considered in this work.

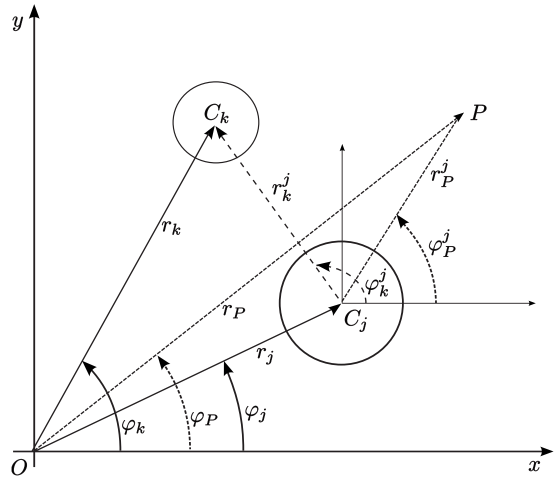

FIG. 1. Schematics of the system geometry. The scattering system consists of N cylinders embedded in a background medium with electric permittivity ϵ_b and magnetic permeability μ_b. The j-th cylinder has radius R_j, permittivity ϵ_j, permeability μ_j, and surface second-order susceptibility $\hat{\chi}_{s,j}^{(2)}$.

A. Description of the system geometry

The nonlinear scattering problem is schematically illustrated in Fig. 1. Thus, we consider an ensemble of N parallel, infinitely long cylinders, C_j, $j=1,2,\ldots,N$, embedded in a background medium with electric permittivity ϵ_b and magnetic permeability μ_b. The cylinders are assumed to be oriented along the z axis. The j-th cylinder has radius R_j and is characterized by the permittivity $\epsilon_j(\omega)$, which, for the sake of generality, is assumed to be dependent on the frequency ω, and the magnetic permeability μ_j; here and in what follows we consider that $\mu_j=\mu_b\equiv\mu_0$, $j=1,2,\ldots,N$, where μ_0 is the magnetic permeability of the vacuum. In addition, each cylinder is characterized by a surface second-order susceptibility, $\hat{\chi}_{s,j}^{(2)}$. The position of the center O_j of the j-th cylinder is specified by the polar coordinates (r_j,φ_j), which are defined with respect to a coordinate system with the origin in O. Moreover, as per Fig. 1, the position of the center of the k-th cylinder, specified in a coordinate system with the origin in O_j, is defined by the polar coordinates (r_k^j,φ_k^j), whereas the position of an arbitrary point P, defined with respect to the coordinate systems with the origin in O and O_j, is specified by the polar coordinates (r_P,φ_P) and (r_P^j,φ_P^j), respectively.

An incident monochromatic electromagnetic plane wave impinging onto the system of cylinders is fully described by its conicity angles ϕ_0, θ_0, and δ_0, where ϕ_0 is the angle between the projection onto the xy plane of the wave vector of the incident wave and the x axis, θ_0 is the angle between the wave vector of the incident wave and the z axis, and δ_0 is the angle between the electric field of the incident wave and the plane defined by the z axis and the wave vector. Moreover, while our analysis can be applied to the general case of oblique incidence, for the sake of simplicity we consider here only the case of normal incidence, i.e., $\theta_0 = \pi/2$. Then, under these circumstances, two independent cases can be considered: in the first case, which corresponds to the transverse electric (TE) polarization, the electric field of the incident wave is perpendicular to the axis of the cylinders ($\delta_0 = \pi/2$), whereas in the case of the transverse magnetic (TM) polarization ($\delta_0 = 0$), the magnetic field of the incident wave is perpendicular to the axis of the cylinders.

B. Calculation of the fields at the fundamental frequency

In order to calculate the fields at both the FF and SH we have employed a method based on the MSM algorithm. This formalism has been successfully used, e.g., to solve the linear scattering problem in the case of oblique incidence of light onto a 2D photonic crystal[42] (for a detailed description of the MSM method see Ref. 43 and the references therein).

Due to the 2D nature of the linear scattering problem considered here, the electromagnetic field at the FF is fully determined once one knows the longitudinal (z) component of either the electric or the magnetic field. To be more specific, for the TM (TE) polarization this longitudinal component is E_z (H_z). Then, using the Maxwell equations, it can be easily shown that for harmonic fields that depend on time as $e^{i\omega t}$, the transverse components are given by

$$H_\varphi = -\frac{i}{\kappa^2}\epsilon\omega\frac{\partial E_z}{\partial r}, \tag{1a}$$

$$H_r = \frac{i}{\kappa^2}\epsilon\omega\frac{1}{r}\frac{\partial E_z}{\partial \varphi}, \tag{1b}$$

for the TM polarization, and

$$E_\varphi = \frac{i}{\kappa^2}\mu_0\omega\frac{\partial H_z}{\partial r}, \tag{2a}$$

$$E_r = -\frac{i}{\kappa^2}\mu_0\omega\frac{1}{r}\frac{\partial H_z}{\partial \varphi}, \tag{2b}$$

for the TE polarization. In these relations, the transverse component of the wave vector, κ, is defined as

$$\kappa^2(\mathbf{r}) = k^2(\mathbf{r}) - k^2\cos^2\theta_0, \tag{3}$$

where $k = \sqrt{\mu_0\epsilon(\mathbf{r})}\omega$ is the wave vector. Depending on the position $\mathbf{r}$ in the transverse plane, $\epsilon(\mathbf{r})$ is equal to either the permittivity of one of the cylinders or to ϵ_b. Also, note that for normal incidence $\kappa = k$, as in this case $\theta_0 = \pi/2$.

In order to simplify the presentation of our numerical method, we assume that all cylinders are made of the same material. In particular, we consider the case of metallic cylinders, their permittivity being described by the Drude model,

$$\epsilon(\omega) = \epsilon_0\left[1 - \frac{\omega_p^2}{\omega(\omega + i\nu)}\right]. \tag{4}$$

Here, ω_p and ν are the plasma and damping frequency, respectively. As specific values for these parameters we choose $\omega_p = 1.35\times10^{16}$ rad/s and $\nu = 2.73\times10^{13}$ s^{-1}, values that correspond to Ag.[44]

Although the technical details can be somewhat complicated, the MSM formalism consists of two simple steps. First, the incident and the scattered electromagnetic fields are expanded in Fourier-Bessel series. Then, the boundary conditions at the surface of the scatterers are used to construct a system of linear equations whose solution determines the Fourier coefficients of the Fourier-Bessel series expansion of the scattered field. Once these coefficients are determined, by solving the corresponding system of linear equations, the electromagnetic field can be found at any point in space. Thus, given an incident plane wave, the longitudinal component of the incoming field, U_z^{inc}, which depending on the polarization of the incoming wave is $U_z^{\mathrm{inc}} = E_z^{\mathrm{inc}}$ ($U_z^{\mathrm{inc}} = H_z^{\mathrm{inc}}$) for TM (TE) polarized waves, can be written as

$$U_z^{\mathrm{inc}}(r,\varphi) = \sum_{m=-\infty}^{\infty} a_m J_m(\kappa_b r)e^{im\varphi}, \tag{5}$$

where J_m denotes the Bessel functions of the first kind. The Fourier coefficients a_m depend solely on the type of the incoming wave, for a plane wave being given by the following formulas:

$$a_m = \begin{cases} E_0 \sin\delta_0 \sin\theta_0 e^{-im(\pi/2+\phi_0)}, & U_z = E_z \\ \dfrac{E_0}{Z_b}\cos\delta_0 \sin\theta_0 e^{-im(\pi/2+\phi_0)}, & U_z = H_z \end{cases}, \tag{6}$$

where $Z_b = \sqrt{\mu_b/\epsilon_b}$ is the impedance of the background medium.

The field scattered by the cylinder C_j can be expanded, too, in a Fourier-Bessel series, but since at $r\to\infty$ the scattered field must contain only outgoing waves, the basis of expansion functions consists of Hankel functions of the second kind, $H_m^{(2)}$. Hence, at a point $P(r,\varphi)$, the field scattered by the cylinder C_j is written as

$$U_{z,j}^{\mathrm{sc}}(r,\varphi) = \sum_{m=-\infty}^{\infty} b_{mj} H_m^{(2)}(\kappa_b r_P^j)e^{im\varphi_P^j}, \tag{7}$$

where b_{mj} are the expansion coefficients and represent the main quantities that are to be determined numerically. It is easy to see now that once the coefficients b_{mj} are computed, the total field at a point P can be readily found. Thus, the field $U_z^{\mathrm{tot}}(P)$ is given by the sum between the incoming field and the fields scattered by all the cylinders,

$$U_z^{\mathrm{tot}}(P) = \sum_{m=-\infty}^{\infty} a_m J_m(\kappa_b r_P)e^{im\varphi_P} + \sum_{j=1}^{N}\sum_{m=-\infty}^{\infty} b_{mj} H_m^{(2)}(\kappa_b r_P^j)e^{im\varphi_P^j}. \tag{8}$$

To find the scattered field we first investigate the source of the field around a cylinder C_j. Thus, this field can be viewed as being generated via scattering off this cylinder of an incoming local field, $U_{z,j}^{\text{loc}}$, which consists of the incoming plane wave and the sum of the fields scattered by all cylinders, except the cylinder C_j. This local field can be written as

$$U_{z,j}^{\text{loc}}(P) = Q_j \sum_{m=-\infty}^{\infty} a_m J_m(\kappa_b r_P^j) e^{im\varphi_P^j} + \sum_{\substack{k=1\\k\neq j}}^{N} \sum_{m,q=-\infty}^{\infty} \mathbf{T}_{jk,mq} b_{qk} J_m(\kappa_b r_P^j) e^{im\varphi_P^j}, \tag{9}$$

where Q_j are phase factors that transform the incoming field from the system with the origin in O to the system with the origin in O_j and $\mathbf{T}_{jk}$ is the electromagnetic coupling matrix between the cylinders j and k. These parameters are defined as[42]

$$Q_j = e^{-i\kappa_b r_j \cos(\varphi_j - \phi_0)}, \tag{10a}$$

$$\mathbf{T}_{jk,mq} = e^{i(q-m)\varphi_k^j} H_{m-q}^{(2)}(\kappa_b r_k^j). \tag{10b}$$

The Eq. (9) can be easily derived by inserting in Eq. (8) the Graf formula[45]

$$H_m^{(2)}(\kappa_b r_P^k) e^{im\varphi_P^k} = \sum_{q=-\infty}^{\infty} e^{i(m-q)\varphi_k^j} H_{q-m}^{(2)}(\kappa_b r_k^j) \times J_q(\kappa_b r_P^j) e^{iq\varphi_P^j}. \tag{11}$$

Now, the local field $U_{z,j}^{\text{loc}}(P)$ can itself be expanded in a Fourier-Bessel series,

$$U_{z,j}^{\text{loc}}(P) = \sum_{m=-\infty}^{\infty} d_{mj} J_m(\kappa_b r_P^j) e^{im\varphi_P^j}. \tag{12}$$

The total field around a cylinder C_j can therefore be written as the sum between this local field and the field scattered by the cylinder [the index j here signifies that $U_z^{\text{tot}}(P)$ is calculated in the system with the origin in O_j]:

$$U_{z,j}^{\text{tot}}(P) = \sum_{m=-\infty}^{\infty} [d_{mj} J_m(\kappa_b r_P^j) + b_{mj} H_m^{(2)}(\kappa_b r_P^j)] e^{im\varphi_P^j}. \tag{13}$$

We introduce now the column vectors $\mathbf{a}_j = \{Q_j a_m\}$, $\mathbf{b}_j = \{b_{mj}\}$, and $\mathbf{d}_j = \{d_{mj}\}$, which contain the Fourier coefficients of the incoming plane wave, the scattered field, and the local field associated to the cylinder C_j, respectively. Furthermore, the scattered field and the local field associated to the cylinder C_j are related by the scattering matrix $\mathbf{S}_j$ of the cylinder C_j, and thus the relation between the vectors $\mathbf{b}_j$ and $\mathbf{d}_j$ is given by

$$\mathbf{b}_j = \mathbf{S}_j \mathbf{d}_j. \tag{14}$$

Combining Eqs. (9), (13), and (14) yields the following linear system of matrix equations:

$$\sum_{k=1}^{N} [\delta_{kj}\mathbf{I} - (1-\delta_{kj})\mathbf{S}_j \mathbf{T}_{jk}] \mathbf{b}_k = \mathbf{S}_j \mathbf{a}_j, \quad j = 1,2,\ldots,N, \tag{15}$$

where δ_{ij} is the Kronecker symbol and $\mathbf{I}$ is the identity matrix. This system of equations can be reduced to a single matrix equation. For this, we stack the column vectors $\mathbf{b}_j$ and $\mathbf{S}_j \mathbf{a}_j$ into the single column vectors $\mathbf{B} = \{\mathbf{b}_j\}$ and $\mathbf{G} = \{\mathbf{S}_j \mathbf{a}_j\}$, respectively, and define the scattering matrix, $\mathbf{S}_\omega$, of the entire system of cylinders as,

$$\mathbf{S}_\omega = \begin{pmatrix} \mathbf{I} & -\mathbf{S}_1\mathbf{T}_{12} & -\mathbf{S}_1\mathbf{T}_{13} & \cdots \\ -\mathbf{S}_2\mathbf{T}_{21} & \mathbf{I} & -\mathbf{S}_2\mathbf{T}_{23} & \cdots \\ -\mathbf{S}_3\mathbf{T}_{31} & -\mathbf{S}_3\mathbf{T}_{32} & \mathbf{I} & \cdots \\ \vdots & \vdots & \vdots & \ddots \end{pmatrix}. \tag{16}$$

With these definitions, Eq. (15) becomes

$$\mathbf{S}_\omega \mathbf{B} = \mathbf{G}. \tag{17}$$

Since the vector $\mathbf{G}$ is known, the linear scattering problem has been reduced to finding the scattering matrix of the system, $\mathbf{S}_\omega$, and then solving the system (17). More exactly, once $\mathbf{S}_\omega$ is determined, the Fourier coefficients $\mathbf{B}$ of the scattered field are calculated by simply solving the linear system (17), the total field at a point P being subsequently determined from Eq. (8). To this end, computing $\mathbf{S}_\omega$ amounts to finding the matrices $\mathbf{S}_j$ of the cylinders C_j, which can be easily determined by using the continuity of the tangent component of the fields across the boundary of the cylinder C_j.

In the case of the TE polarization, the boundary conditions can be expressed as

$$H_{z,j}^{\text{ext}}(R_j,\varphi) = H_{z,j}^{\text{int}}(R_j,\varphi), \tag{18a}$$

$$E_{\varphi,j}^{\text{ext}}(R_j,\varphi) = E_{\varphi,j}^{\text{int}}(R_j,\varphi). \tag{18b}$$

The magnetic field inside the cylinder C_j, $H_{z,j}^{\text{int}}$, can be written as

$$H_{z,j}^{\text{int}}(P) = \sum_{m=-\infty}^{\infty} c_{mj} J_m(\kappa_j r_P^j) e^{im\varphi_P^j}, \tag{19}$$

whereas the tangent component of the electric field, $E_{\varphi,j}^{\text{int}}$, is determined from the Eq. (2a). Using the Eq. (13), imposing the continuity conditions (18), and eliminating the coefficients c_{mj} from the resulting system of equations, one obtains the following relation between the b_{mj} and d_{mj} coefficients:

$$\frac{b_{mj}}{d_{mj}} = \frac{\beta_j J_m'(\kappa_b R_j) J_m(\kappa_j R_j) - J_m(\kappa_b R_j) J_m'(\kappa_j R_j)}{H_m^{(2)}(\kappa_b R_j) J_m'(\kappa_j R_j) - \beta_j H_m^{(2)\prime}(\kappa_b R_j) J_m(\kappa_j R_j)}. \tag{20}$$

Here, the prime symbol denotes the derivative with respect to the argument and $\beta_j = \kappa_j / \kappa_b$. These calculations can be repeated for the case of the TM polarization, the result being that Eq. (20) remains valid, but in this case $\beta_j = (\epsilon_b \kappa_j)/(\epsilon_j \kappa_b)$. Now, the definition (14) shows that $S_{j,mn} = (b_{mj}/d_{mj})\delta_{mn}$, which means that for cylinders, in the case of a TE or TM polarized incident wave, the scattering matrix is diagonal. Importantly, by using the same procedure one can obtain a relation between b_{mj} and c_{mj}, which is similar to the Eq. (20). With the Fourier coefficients now known, the field inside the cylinders can be determined by using Eq. (19). Note that this formalism can be easily extended to the case of scatterers of arbitrary shape, the main difference being that in this case the scattering matrices $\mathbf{S}_j$ are no longer diagonal.[46]

C. Calculation of the fields at the second harmonic

The second step of our numerical method consists in the calculation of the electromagnetic field at the SH. To this end, we first determine the source of the field at the SH, namely, the nonlinear polarization induced by the field at the FF. According to a model that is widely used in the study of the SHG in centrosymmetric media,[47] this nonlinear polarization can be separated in two distinct components. First, a (local) dipole-allowed surface nonlinear polarization, $\mathbf{P}_s(\mathbf{r};2\omega)$, whose support is a surface layer several Ångströms thin, and the second, a (nonlocal) bulk nonlinear polarization, $\mathbf{P}_b(\mathbf{r};2\omega)$, which is generated inside the nonlinear medium by electric quadrupoles and magnetic dipoles.

The surface polarization vector is defined as

$$\mathbf{P}_s(\mathbf{r};2\omega) = \epsilon_0 \hat{\chi}_s^{(2)}:\mathbf{E}(\mathbf{r};\omega)\mathbf{E}(\mathbf{r};\omega)\delta(\mathbf{r}-\mathbf{r}_s), \tag{21}$$

where $\mathbf{r}_s$ defines the surface, $\hat{\chi}_s^{(2)}$ is the surface second-order susceptibility tensor, and the Dirac function shows the surface characteristic of this source nonlinear polarization. Unless the surface contains structural features with intrinsic chirality, the metal/background interfaces possess an isotropic mirror-symmetry plane perpendicular to the interface. Under these circumstances, the surface nonlinear susceptibility $\hat{\chi}_s^{(2)}$ has only three independent components, namely, $\hat{\chi}_{s,\perp\perp\perp}^{(2)}$, $\hat{\chi}_{s,\perp\parallel\parallel}^{(2)}$, and $\hat{\chi}_{s,\parallel\parallel\perp}^{(2)}=\hat{\chi}_{s,\parallel\perp\parallel}^{(2)}$, where the symbols $\perp$ and $\parallel$ refer to the directions normal and tangent to the surface, respectively. In our calculations, we assume that the cylinders are made of Ag, and thus we use $\hat{\chi}_{s,\perp\perp\perp}^{(2)}=2.79\times10^{-18}\ \mathrm{m}^2/\mathrm{V}$, $\hat{\chi}_{s,\parallel\parallel\perp}^{(2)}=\hat{\chi}_{s,\parallel\perp\parallel}^{(2)}=3.98\times10^{-20}\ \mathrm{m}^2/\mathrm{V}$, and $\hat{\chi}_{s,\perp\parallel\parallel}^{(2)}=0$.[48]

From the symmetry properties of the surface susceptibility tensor $\hat{\chi}_s^{(2)}$ one can derive the polarization characteristics of the field at the SH, which is generated by the surface nonlinear polarization. Thus, in the case of the TM polarization the normal component of the electric field is zero and consequently no field is generated at the SH. On the other hand, when the incident wave is TE polarized, the electric field lies in the transverse plane, and thus the field at the surface of the cylinders contains both normal and tangent components. Specifically, the nonlinear surface polarization has the following components:

$$P_{s,r} = \epsilon_0 \hat{\chi}_{s,\perp\perp\perp}^{(2)} E_r^2, \tag{22a}$$

$$P_{s,\varphi} = 2\epsilon_0 \hat{\chi}_{s,\parallel\perp\parallel}^{(2)} E_r E_\varphi. \tag{22b}$$

The nonlinear bulk polarization in an isotropic centrosymmetric medium has the following general expression:[49]

$$\mathbf{P}_b(2\omega) = \alpha[\mathbf{E}(\omega)\cdot\nabla]\mathbf{E}(\omega) + \beta\mathbf{E}(\omega)[\nabla\cdot\mathbf{E}(\omega)] + \gamma\nabla[\mathbf{E}(\omega)\cdot\mathbf{E}(\omega)], \tag{23}$$

where α, β, and γ are the bulk nonlinear coefficients of the material. If we assume that the electrons in the metal are described by the free-electron model, these parameters are

$$\alpha = 0, \tag{24a}$$

$$\beta = \epsilon_0 \frac{e}{2m_0\omega^2}, \tag{24b}$$

$$\gamma = \frac{\beta}{4}[1-\epsilon_r(\omega)], \tag{24c}$$

with e and m_0 being the electron charge and mass, respectively, and $\epsilon_r(\omega)=\epsilon(\omega)/\epsilon_0$ the relative permittivity of the metal. As we will show in what follows, the SHG is dominated by the surface component, which in turn is generated only in the case of the TE polarization. As a result, we will consider only this case. Furthermore, it should be noted that the free electrons in the metal also contribute to the nonlinear surface susceptibility (primarily to the component $\hat{\chi}_{s,\perp\perp\perp}^{(2)}$), but this contribution is already accounted for by the experimentally determined values of the components of the nonlinear surface susceptibility.[48]

The nonlinear boundary conditions obeyed by the electromagnetic fields at the SH, in the case of the TE polarization, are given by[47]

$$H_z^{\mathrm{int}}(\Omega) - H_z^{\mathrm{ext}}(\Omega) = i\Omega P_{s,\varphi}, \tag{25a}$$

$$\frac{1}{\epsilon_j}D_\varphi^{\mathrm{int}}(\Omega) - \frac{1}{\epsilon_b}D_\varphi^{\mathrm{ext}}(\Omega) = -\frac{1}{\epsilon_j R_j}\frac{\partial P_{s,r}}{\partial\varphi} + \frac{P_{b,\varphi}}{\epsilon_j}, \tag{25b}$$

where the permittivities are evaluated at the SH frequency $\Omega=2\omega$. Note that due to the presence of the nonlinear polarization sheet at the surface of the metal the nonlinear boundary conditions are different from the linear ones, which are given by the Eqs. (18).

Similar to the linear scattering problem, the total SH field at a point P can be viewed as consisting of two distinct components: a source field, $H_z^{\mathrm{src}}(P,\Omega)$, which reaches the point P without being scattered by any of the cylinders, and the scattered field, $H_z^{\mathrm{sc}}(P,\Omega)$, which arrives at P after it was scattered by at least one of the cylinders,

$$H_z^{\mathrm{tot}}(P,\Omega) = H_z^{\mathrm{src}}(P,\Omega) + H_z^{\mathrm{sc}}(P,\Omega). \tag{26}$$

The source field satisfies the Helmholtz equation

$$\nabla^2 H_z^{\mathrm{src}}(\mathbf{r};\Omega) + \kappa_b^2(\Omega)H_z^{\mathrm{src}}(\mathbf{r},\Omega) = -i\Omega(\nabla\times\mathbf{P}_{\mathrm{nl}})\cdot\mathbf{e}_z, \tag{27}$$

where $\mathbf{e}_z$ is the unit vector along the z axis and $\mathbf{P}_{\mathrm{nl}}=\mathbf{P}_s+\mathbf{P}_b$ is the total nonlinear polarization. Since the source polarization $\mathbf{P}_{\mathrm{nl}}$ is known once the electric field at the FF is determined, this source field can easily be calculated by using the Green function of the Helmholtz equation in 2D, $G_{2D}(r)=-(i/4)H_0^{(2)}(r)$,

$$H_z^{\mathrm{src}}(P,\Omega) = -\frac{\Omega}{4} H_0^{(2)}(\kappa_b r_P) \otimes [(\nabla \times \mathbf{P}_{\mathrm{nl}}) \cdot \mathbf{e}_z]. \quad (28)$$

In this equation the symbol $\otimes$ represents the convolution operator. Because of the particular characteristics of the surface and bulk polarizations, the Eq. (28) represents the sum between a line integral over the boundaries of all cylinders and a surface integral over their transverse cross sections. Moreover, the field $H_z^{\mathrm{src}}(P,\Omega)$ consists of a linear superposition of fields $H_{z,j}^{\mathrm{src}}(P,\Omega)$, each such field being generated by the corresponding cylinder C_j. Inserting in the Eq. (28) the Graf formula[45] for the Bessel function $H_0^{(2)}(r)$,

$$H_0^{(2)}(\kappa_b|\mathbf{r}_P - \mathbf{r}_M|) = \sum_{m=-\infty}^{\infty} e^{-im\varphi_M^j} J_m(\kappa_b r_M^j) \times H_m^{(2)}(\kappa_b r_P^j) e^{im\varphi_P^j}, \quad (29)$$

one can easily show that the Fourier-Bessel expansion of the field $H_{z,j}^{\mathrm{src}}(P,\Omega)$, around the cylinder C_j, can be written as

$$H_{z,j}^{\mathrm{src}}(P) = \sum_{m=-\infty}^{\infty} a_{\Omega,mj} H_m^{(2)}(\kappa_b r_P^j) e^{im\varphi_P^j}, \quad (30)$$

where,

$$a_{\Omega,mj} = -\frac{\Omega}{4} \int_{\Gamma_j} e^{-im\varphi_M^j} J_m(\kappa_b r_M^j) [(\nabla_{\mathbf{r}_M^j} \times \mathbf{P}_{\mathrm{nl}}) \cdot \mathbf{e}_z] d\mathbf{r}_M^j. \quad (31)$$

In this relation, the domain of integration Γ_j is either the boundary of the cylinder C_j, in the case of the surface polarization, or its transverse cross section, when the bulk polarization is integrated. Similar to our analysis of the scattering process at the FF, the scattered field at the SH can be written as [see also the Eq. (8)]

$$H_z^{\mathrm{sc}}(P,\Omega) = \sum_{j=1}^{N} \sum_{m=-\infty}^{\infty} b_{\Omega,mj} H_m^{(2)}(\kappa_b r_P^j) e^{im\varphi_P^j}, \quad (32)$$

where $b_{\Omega,mj}$ are the scattering coefficients at the SH. Combining Eqs. (30) and (32) leads to the formula for the total field $H_z^{\mathrm{tot}}(P,\Omega)$,

$$H_z^{\mathrm{tot}}(P,\Omega) = \sum_{j=1}^{N} \sum_{m=-\infty}^{\infty} (a_{\Omega,mj} + b_{\Omega,mj}) H_m^{(2)}(\kappa_b r_P^j) e^{im\varphi_P^j}, \quad (33)$$

where the two series containing the $a_{\Omega,mj}$ and $b_{\Omega,mj}$ coefficients correspond to the source and scattered fields, respectively. By inserting in this equation the Graf formula (11), the total field outside the cylinder C_j, at a point P, can be written in the following form:

$$H_{z,j}^{\mathrm{tot}}(P,\Omega) = \sum_{m=-\infty}^{\infty} (a_{\Omega,mj} + b_{\Omega,mj}) H_m^{(2)}(\kappa_b r_P^j) e^{im\varphi_P^j} + \sum_{\substack{k=1\\k\neq j}}^{N} \sum_{m,q=-\infty}^{\infty} T_{jk,mq}(a_{\Omega,qk} + b_{\Omega,qk}) J_m(\kappa_b r_P^j) e^{im\varphi_P^j}, \quad (34)$$

where the index j signifies that $H_z^{\mathrm{tot}}(P,\Omega)$ is calculated in the coordinate system with the origin in O_j. This equation shows that the total field consists of the sum between the field generated and scattered by the cylinder C_j [the first term in the Eq. (34)] and the total field incident onto this cylinder [the second term in the Eq. (34)]. This latter field, in turn, is given by the sum between the fields generated by all the other cylinders and the fields scattered by these cylinders.

The total field can also be decomposed in an alternative way, namely, it can be written as the sum of a source field generated by the cylinder C_j, $H_{z,j}^{\mathrm{self}}(P,\Omega)$, a local field, $H_{z,j}^{\mathrm{loc}}(P,\Omega)$, which is the field incident onto C_j, and the corresponding scattered field, $H_{z,j}^{\mathrm{sc}}(P,\Omega)$. Furthermore, we require that the source field satisfies the nonlinear boundary conditions (25), whereas the field involved in the scattering process,

$$H_{z,j}^{\mathrm{lin}}(P,\Omega) = H_{z,j}^{\mathrm{loc}}(P,\Omega) + H_{z,j}^{\mathrm{sc}}(P,\Omega), \quad (35)$$

satisfies the linear boundary conditions corresponding to the TE polarization, i.e., Eqs. (18). It should be noted that if the nonlinear bulk polarization is given by the Eq. (23) then the source term in the Helmholtz Eq. (27) cancels everywhere except on the boundaries of the cylinders and therefore the fields $H_{z,j}^{\mathrm{self}}(P,\Omega)$ and $H_{z,j}^{\mathrm{lin}}(P,\Omega)$ satisfy the homogeneous part of this equation.

Now, the source field can be expanded in Fourier-Bessel series as

$$H_{z,j}^{\mathrm{self}}(P,\Omega) = \sum_{m=-\infty}^{\infty} c_{\Omega,mj}^{\mathrm{self}} J_m(\kappa_j r_P^j) e^{im\varphi_P^j}, \quad (36)$$

for $r_P^j < R_j$, and

$$H_{z,j}^{\mathrm{self}}(P,\Omega) = \sum_{m=-\infty}^{\infty} g_{\Omega,mj}^{\mathrm{self}} H_m^{(2)}(\kappa_b r_P^j) e^{im\varphi_P^j}, \quad (37)$$

for $r_P^j > R_j$. By imposing the nonlinear boundary conditions (24d) at $r_P^j = R_j$, we obtain the following system of linear equations for the coefficients $c_{\Omega,mj}^{\mathrm{self}}$ and $g_{\Omega,mj}^{\mathrm{self}}$:

$$c_{\Omega,mj}^{\mathrm{self}} J_m(\kappa_j R_j) - g_{\Omega,mj}^{\mathrm{self}} H_m^{(2)}(\kappa_b R_j) = i\Omega \bar{P}_{\varphi,m}, \quad (38a)$$

$$\frac{i\kappa_j}{\epsilon_j \Omega} c_{\Omega,mj}^{\mathrm{self}} J_m'(\kappa_j R_j) - \frac{i\kappa_b}{\epsilon_b \Omega} g_{\Omega,mj}^{\mathrm{self}} H_m^{(2)\prime}(\kappa_b R_j) = \bar{P}_{r,m}. \quad (38b)$$

In these relations,

$$\bar{P}_{\varphi,m} = P_{s\varphi,m}, \quad (39a)$$

$$\bar{P}_{r,m} = -\frac{1}{\epsilon_j R_j}\frac{\partial P_{sr,m}}{\partial \varphi}\bigg|_{r_P^j=R_j} + \frac{P_{b\varphi,m}}{\epsilon_j}. \tag{39b}$$

are the m-th order coefficients of the expansion in Fourier-Bessel series of the nonlinear polarization. The solution of the linear system (38), which completely determine the source field $H_{z,j}^{\text{self}}(P,\Omega)$, is found as

$$c_{\Omega,mj}^{\text{self}} = i\frac{\Upsilon_{c,m}}{\Delta_m}, \tag{40a}$$

$$g_{\Omega,mj}^{\text{self}} = i\frac{\Upsilon_{g,m}}{\Delta_m}, \tag{40b}$$

where $\Upsilon_{c,m}=H_m^{(2)}(k_bR_j)\bar{P}_{r,m}+Z_bH_m^{(2)\prime}(k_bR_j)\Omega\bar{P}_{\varphi,m}$, $\Upsilon_{g,m}=J_m(\kappa_jR_j)\bar{P}_{r,m}+Z_jJ_m'(\kappa_jR_j)\Omega\bar{P}_{\varphi,m}$, $\Delta_m=Z_bJ_m(\kappa_jR_j)H_m^{(2)\prime}(\kappa_bR_j)-Z_jH_m^{(2)}(\kappa_bR_j)J_m'(\kappa_jR_j)$, and $Z_j=(\mu_j/\epsilon_j)^{1/2}$. Note that these coefficients can be easily calculated once the FF field is determined. Based on the Eq. (35), the field $H_{z,j}^{\text{lin}}(P,\Omega)$ can be written as

$$H_{z,j}^{\text{lin}}(P,\Omega) = \sum_{m=-\infty}^{\infty} c_{\Omega,mj}^{\text{lin}} J_m(\kappa_j r_P^j) e^{im\varphi_P^j}, \tag{41}$$

for $r_P^j<R_j$ and

$$H_{z,j}^{\text{lin}}(P,\Omega) = \sum_{m=-\infty}^{\infty} f_{\Omega,mj}^{\text{loc}} J_m(\kappa_b r_P^j) e^{im\varphi_P^j} + \sum_{m=-\infty}^{\infty} g_{\Omega,mj}^{\text{sc}} H_m^{(2)} \times(\kappa_b r_P^j) e^{im\varphi_P^j}, \tag{42}$$

for $r_P^j>R_j$. Now, by combining Eqs. (37) and (42) one can cast the total field $H_{z,j}^{\text{tot}}(P,\Omega)$ outside the cylinder C_j in the following form:

$$H_{z,j}^{\text{tot}}(P,\Omega) = \sum_{m=-\infty}^{\infty} f_{\Omega,mj}^{\text{loc}} J_m(\kappa_b r_P^j) e^{im\varphi_P^j} + \sum_{m=-\infty}^{\infty} (g_{\Omega,mj}^{\text{self}} + g_{\Omega,mj}^{\text{sc}}) H_m^{(2)}(\kappa_b r_P^j) e^{im\varphi_P^j}, \tag{43}$$

We now introduce the vectors $\mathbf{a}_{\Omega,j}=\{a_{\Omega,mj}\}$, $\mathbf{b}_{\Omega,j}=\{b_{\Omega,mj}\}$, $\mathbf{g}_{\Omega,j}^{\text{self}}=\{g_{\Omega,mj}^{\text{self}}\}$, $\mathbf{g}_{\Omega,j}^{\text{sc}}=\{g_{\Omega,mj}^{\text{sc}}\}$, and $\mathbf{f}_{\Omega,j}=\{f_{\Omega,mj}^{\text{loc}}\}$. Then, by comparing Eqs. (34) and (43), one can see that these vectors satisfy the following relations:

$$\mathbf{a}_{\Omega,j} + \mathbf{b}_{\Omega,j} = \mathbf{g}_{\Omega,j}^{\text{self}} + \mathbf{g}_{\Omega,j}^{\text{sc}}, \tag{44a}$$

$$\sum_{\substack{k=1\\k\neq j}}^{N} \mathbf{T}_{jk}(\mathbf{a}_{\Omega,k} + \mathbf{b}_{\Omega,k}) = \mathbf{f}_{\Omega,j}. \tag{44b}$$

Furthermore, the scattered and the incident (local) fields are related via the scattering matrix $\mathbf{S}_{\Omega,j}$,

$$\mathbf{g}_{\Omega,j}^{\text{sc}} = \mathbf{S}_{\Omega,j}\mathbf{f}_{\Omega,j}, \tag{45}$$

where the index Ω means that the scattering matrix is evaluated at the frequency of the SH. From this equation and Eqs. (44) we can derive the relation

$$\sum_{\substack{k=1\\k\neq j}}^{N} \mathbf{S}_{\Omega,j}\mathbf{T}_{jk}(\mathbf{a}_{\Omega,k} + \mathbf{b}_{\Omega,k}) = (\mathbf{a}_{\Omega,j} + \mathbf{b}_{\Omega,j}) - \mathbf{g}_{\Omega,j}^{\text{self}}, \tag{46}$$

which holds for $j=1,\ldots,N$. This linear system of matrix equations can be written in a more compact form if we introduce the vectors $\mathbf{A}_\Omega=\{\mathbf{a}_{\Omega,j}\}$, $\mathbf{B}_\Omega=\{\mathbf{b}_{\Omega,j}\}$, and $\mathbf{G}_\Omega^{\text{self}}=\{\mathbf{g}_{\Omega,j}^{\text{self}}\}$. With these notations, the Eq. (46) becomes

$$\mathbf{S}_\Omega\mathbf{B}_\Omega = \mathbf{G}_\Omega, \tag{47}$$

where $\mathbf{S}_\Omega$ is given by the Eq. (16), with all matrix components evaluated at the frequency Ω, and

$$\mathbf{G}_\Omega = -\mathbf{S}_\Omega\mathbf{A}_\Omega + \mathbf{G}_\Omega^{\text{self}}. \tag{48}$$

The vector coefficients $\mathbf{A}_\Omega$ and $\mathbf{G}_\Omega^{\text{self}}$ are completely determined once the field at the FF is calculated. As a result, the scattering vector coefficients $\mathbf{B}_\Omega$ can be found by solving the system (47), and subsequently the field at a point P outside the cylinders is determined from the Eq. (33).

Finally, it can be seen from Eqs. (36) and (41) that the total field inside the cylinder C_j is given by the following equation:

$$H_{z,j}^{\text{tot}}(P,\Omega) = \sum_{m=-\infty}^{\infty} (c_{\Omega,mj}^{\text{self}} + c_{\Omega,mj}^{\text{lin}}) J_m(\kappa_j r_P^j) e^{im\varphi_P^j}. \tag{49}$$

As in the case of the linear scattering problem, the coefficients $c_{\Omega,mj}^{\text{lin}}$ are calculated by imposing on the field $H_{z,j}^{\text{lin}}(P,\Omega)$ the linear boundary conditions (18).

D. Technical Implementation of the numerical method

Because of the nature of the MSM method, the numerical algorithm lends itself to a very efficient, parallel implementation, as many of the major computational steps are independent of each other. The main steps in the simulation are as follows. First, the scattering matrices, $\mathbf{S}_j$, of single cylinders are calculated and subsequently the scattering matrix at the FF, $\mathbf{S}_\omega$, is determined using the Eq. (16). The scattering coefficients at the FF are then found by solving the linear system given by the Eq. (17). These coefficients are used to determine the fields at the FF, via the Eq. (8), which are then used to compute by means of the Eqs. (21) and (23) the total nonlinear polarization at the SH. Note that in the calculations presented here we used all components of the nonlinear surface susceptibility tensor (not only the dominant one, $\hat{\chi}_{s,\perp\perp\perp}^{(2)}$) whereas for the bulk nonlinear polarization we used the Drude model (24). Furthermore, once one knows the total nonlinear polarization at the SH one can determine the source coefficients, $\mathbf{A}_\Omega$, and the vector $\mathbf{G}_\Omega^{\text{self}}$, and, implicitly, the vector $\mathbf{G}_\Omega$. Then, the scattering coefficients and the fields at the SH are determined from the Eq. (47) and (33), respectively. Finally, the fields inside the cylinders, at the FF and SH, are calculated by using the Eqs. (19), (36), and (41).

There is a series of numerical parameters that need to be determined so that the numerical results converge. The most important of these parameters is the number M of Bessel and Hankel functions used in the Fourier-Bessel expansions. Due to the technical limitations imposed by the 64 bit data storage, the order m is restricted to 120, leading to a maximum of $M=241$ expansion terms. Nevertheless, our numerical tests have shown that, for example, for a one cylinder ($R=500$ nm) geometry case, convergence can be achieved by employing $M\approx 41$ expansion terms. On the other hand, for the most complex of the scattering geometries studied here convergence is reached at $M\approx 81$. Other numerical parameters required for the implementation of the MSM method are related to the numerical integrations needed to determine the nonlinear source coefficients, $\mathbf{A}_{\Omega}$, and the absorption cross section. Thus, the numerical integration has been performed by uniformly dividing the $[0,2\pi]$ domain into 360 intervals and the $[0,R_j]$ domains into 20 intervals. Integration was performed using a fourth-order Simpson formula.

The code has been developed and run on a high-performance computing system of Intel®Xeon processors using the Message Passing Interface to assure parallelization. In addition, in order to solve the system of linear equations that gives the scattering coefficients at the FF and SH we have employed linear algebra solvers in the [Intel® Math Kernel Library]. Typical runtimes using 32 cores are about 15 min for computing just the field profile at a fixed wavelength and can run to about 1 h for scanning over 800 distinct wavelengths while computing only the cross sections of the scattering system.

III. CALCULATION OF THE TOTAL, ABSORPTION, AND SCATTERING CROSS SECTION

The MSM formalism allows one to determine not only the spatial distribution of the electromagnetic field but also a series of important physical quantities, such as the total cross section, the absorption cross section, and the scattering cross section. Whereas the field distribution provides essential information regarding the properties of the optical near field, the scattering cross sections characterize the process of energy transfer from the incident wave into the far-field.

A. Calculation of scattering cross sections

The total scattering cross section, $Q_s(\omega)$, for the field at the FF is defined as

$$Q_s(\omega) \equiv \frac{P^{\mathrm{sc}}(\omega)}{P^{\mathrm{inc}}} = \int_0^{2\pi} q_s(\varphi;\omega)d\varphi, \tag{50}$$

where P^{sc} and P^{inc} are the total scattered power per unit length and the power per unit length of the incident wave, respectively, and $q_s(\varphi;\omega)$ is the differential cross section.

In order to calculate the total scattered power we consider a cylinder of radius R, which contains all the scatterers, and compute the total power of the scattered field that flows through the boundary of this cylinder. Then, R is increased to infinity and the corresponding asymptotic value of P^{sc} is determined. This procedure is expressed mathematically as follows:

$$P^{\mathrm{sc}}(\omega) = \lim_{R\to\infty}\left[R\int_0^{2\pi}\frac{1}{2}\mathfrak{Re}(\mathbf{E}^{\mathrm{sc}}\times\mathbf{H}^{\mathrm{sc}^*})_r d\varphi\right]. \tag{51}$$

By using the asymptotic expressions at $x\to\infty$, of the Hankel functions $H_m^{(2)}(x)$ and their derivatives, we obtain

$$P^{\mathrm{sc}}(\omega) = \frac{\mu_b\omega}{\pi\kappa_b^2}\int_0^{2\pi}\left|\sum_{m=-\infty}^{\infty}\tilde{b}_m e^{im\varphi}\right|^2 d\varphi, \tag{52}$$

where $\tilde{b}_{mj}$ are the scattering coefficients in the coordinate system with the origin in O. Using the Graf formula, these coefficients can be written as

$$\tilde{b}_m = \sum_{j=0}^{N}\sum_{n=-\infty}^{\infty} b_{mj}e^{i(n-m)\varphi_j}J_{m-n}(\kappa_b r_j). \tag{53}$$

Furthermore, the power per unit length of the incident plane wave is given by

$$P^{\mathrm{inc}} = \frac{1}{2}R_s v\epsilon_b|E_0|^2, \tag{54}$$

where R_s is the radius of the smallest cylinder that would contain the entire set of scatterers and v is the phase velocity of the incident plane wave. Note that since the amplitude of the scattered field depends linearly on the amplitude E_0 of the incident plane wave, the total and the differential scattering cross sections do not depend on E_0. In order to have this condition satisfied at the SH, too, we define the scattering cross sections at Ω as

$$Q_s(\Omega) \equiv \frac{P^{\mathrm{sc}}(\Omega)}{|P^{\mathrm{inc}}|^2} = \int_0^{2\pi} q_s(\varphi;\Omega)d\varphi. \tag{55}$$

B. Calculation of the absorption cross section

The scattering cross section characterizes the strength of the interaction between incoming plane waves and the objects that scatter these waves. Another physical quantity that provides insightful information about the scattering process is the absorption cross section. In particular, the absorption cross section quantifies the rate at which the scattering system absorbs energy from the incident wave, and as such it can be instrumental in characterizing the strength of the coupling between the near field and the system of scatterers. At the FF, the absorption cross section can be determined by separating the total power flow out of the scattering region, P^{tot}, which sometimes is also referred to as the "extinction" power, into the absorbed and scattered power,

$$P^{\mathrm{tot}} = P^{\mathrm{abs}} + P^{\mathrm{sc}}. \tag{56}$$

In this equation, P^{tot} is defined as

$$P^{\mathrm{tot}}(\omega) = \lim_{R\to\infty}\left[R\int_0^{2\pi}\frac{1}{2}\mathfrak{Re}(\mathbf{E}^{\mathrm{tot}}\times\mathbf{H}^{\mathrm{tot}^*})_r d\varphi\right]. \tag{57}$$

Taking into account that $\mathbf{E}^{\mathrm{tot}}=\mathbf{E}^{\mathrm{inc}}+\mathbf{E}^{\mathrm{sc}}$ and $\mathbf{H}^{\mathrm{tot}}=\mathbf{H}^{\mathrm{inc}}+\mathbf{H}^{\mathrm{sc}}$, the Eq. (57), in conjunction with the Eq. (51), leads to the following expression for the total power:[50]

$$P^{\mathrm{tot}} = -\lim_{R\to\infty}\left[R\int_0^{2\pi}\frac{1}{2}\mathfrak{Re}(E_\varphi^{\mathrm{sc}}H_z^{\mathrm{inc}^*} + E_\varphi^{\mathrm{inc}}H_z^{\mathrm{sc}^*})d\varphi\right]. \tag{58}$$

Using again the asymptotic forms for the Bessel and Hankel functions, the total power can be expressed as

$$P^{\mathrm{tot}} = -\frac{2\mu_b\omega}{\kappa_b^2 Z_b}\sum_{m=-\infty}^{\infty}|\tilde{b}_m|\cos\left(\arg\tilde{b}_m + \frac{m\pi}{2} + m\varphi_0\right). \quad (59)$$

This total power is used to define the total (or extinction) cross section,

$$Q_t(\omega) = \frac{P^{\mathrm{tot}}(\omega)}{P^{\mathrm{inc}}}. \quad (60)$$

Similarly, the absorption cross section is defined as,

$$Q_a(\omega) = \frac{P^{\mathrm{abs}}(\omega)}{P^{\mathrm{inc}}}. \quad (61)$$

Finally, by using the Eq. (56), the absorption cross section is simply given by

$$Q_a(\omega) = Q_t(\omega) - Q_s(\omega). \quad (62)$$

It should be noted that when the scatterers exhibit no absorption, i.e., when $\nu=0$, the absorption cross section vanishes, in which case Eq. (62) represents the well known optical theorem.

In the case of the SH, as there is no incoming field, the approach just described cannot be used to calculate the total cross section. The power loss per unit length, in this case, is determined by integrating over the transverse cross section of all cylinders the Joule thermal power loss, $P^{\mathrm{abs}} = \frac{1}{2}\mathfrak{Re}(\mathbf{J}\cdot\mathbf{E}^*)$, with $\mathbf{J}=\sigma_j\mathbf{E}$ being the conduction current density and σ_j the conductivity of the cylinder C_j (for the Drude model, $\sigma=(\epsilon_0\omega_p^2)/(\nu-i\omega)$).

IV. LINEAR AND NONLINEAR SCATTERING FROM METALLIC CYLINDERS

In this section we apply the numerical method just described to investigate the linear and nonlinear scattering from a set of homogeneous centrosymmetric (metallic) cylinders. We consider several cases that are of particular practical interest, namely, scattering by one cylinder, scattering by 1D chains of cylinders, and the general case of wave scattering by 2D ordered and random distributions of cylinders.

A. Second harmonic generation from a single metallic cylinder

To begin with, let us consider the linear and nonlinear wave scattering by a single metallic cylinder. This is an important case because it has an analytical solution,[40] which allows us to validate our numerical method. We have therefore considered the wave scattering by a cylinder with radius $R=500$ nm and calculated the scattering cross section, at both the FF and at the SH. The results of these calculations, which are presented in Fig. 2, show that the scattering cross section at the FF has a global maximum at the wavelength $\lambda\sim300$ nm, whereas the scattering cross section at the SH decreases with the wavelength. In addition, it can be seen that the scattering cross sections at the FF and SH present a series of spectral peaks. Note that at the FF there is only one set of such spectral resonances; however, at the SH there are two spectral regions in which the scattering cross section presents a series of spectral peaks. As we will explain in more detail later, the physical origin of these two sets of spectral peaks at the SH can be traced to different physical effects.

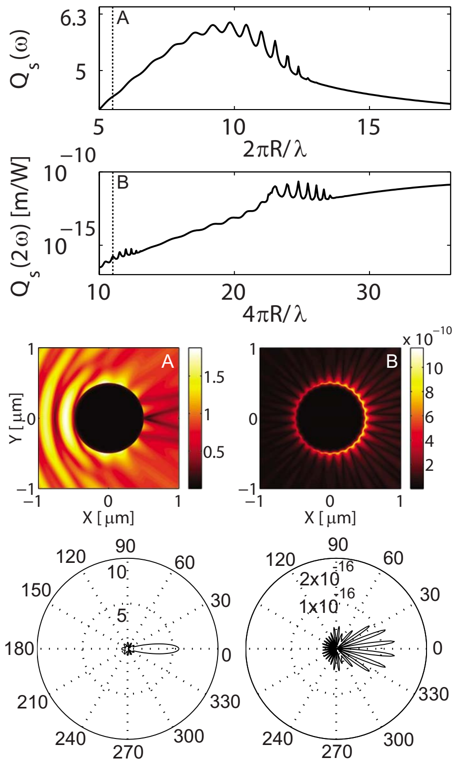

FIG. 2. (Color online) The top two panels show the logarithmic plot of the total scattering cross sections corresponding to a single cylinder with radius $R=500$ nm. The panels in the middle show the spatial distribution of the electric field amplitude calculated at $\lambda=570$ nm and correspond to the dashed vertical lines in the top two panels. The bottom panels present the polar representation of the differential scattering cross sections, calculated at the same wavelength $\lambda=570$ nm. Left and right panels correspond to the FF and SH, respectively.

The properties of the maxima in Fig. 2 are revealed, in part, by the spatial distribution of the amplitude of the electric field, calculated at the wavelength of these spectral peaks. Thus, Fig. 2 shows that at $\lambda=525$ nm, which corresponds to one of the maxima of $Q_s(\Omega)$, the amplitude of the electric field around the cylinder, at the SH, presents a series of local maxima (see panel B in Fig. 2). This is a signature of the excitation of localized surface plasmon modes.[51] These are TE modes of the metallic cylinder, at their cut-off wavelength. To be more specific, since the wave vector of the incident wave is perpendicular to the axis of the cylinder, the propagation constant of the waveguide modes of the cylinder must be zero, i.e., it satisfies the cut-off condition. Note that for this wavelength no SPPs are excited at the FF.

There is also an obvious relation between the spatial distribution of the near field at the SH and the scattering pattern showed by the differential scattering cross section, $q_s(\varphi;\Omega)$. Thus, the polar representation of $q_s(\varphi;\Omega)$, shown in Fig. 2, reveals that the SH is radiated primarily along a series of specific directions, the number of these angular maxima being equal to the number of maxima of the spatial distribution

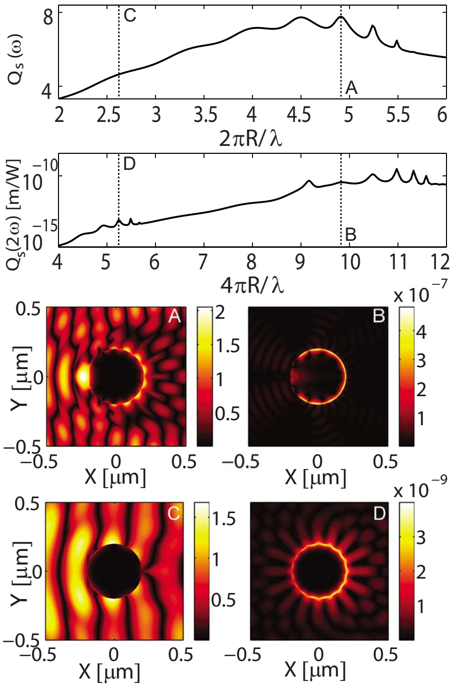

FIG. 3. (Color online) The top panels show the spectra of the scattering cross sections. The spatial profile of the amplitude of the electric field, calculated at the wavelength $\lambda=257$ nm (A and B) and $\lambda=480$ nm (C and D), are plotted in the bottom panels. The radius of the cylinder is $R=200$ nm. Left and right panels correspond to the FF and SH, respectively.

of the near field. As a general characteristic of the scattering pattern at the SH, most of the radiation is emitted in the forward direction. At the FF most of the radiation is primarily emitted in the forward direction, too, although there are several other secondary directions in which a much smaller amount of radiation is emitted. It should be noted that these results obtained by numerical simulations fully agree with the analytical solution of the linear and nonlinear scattering problem, which is presented in Ref. 40.

We also consider this same scattering process, but for a cylinder with $R=200$ nm. The main results obtained in this case are summarized in Fig. 3. It can be seen in this figure that by decreasing the radius of the cylinder the number of SPP modes of the cylinder decreases and their resonance wavelength is blue shifted. Figure 3 also provides additional physical insight into the nature of the two different types of SPP resonances excited at the SH. The origin of the first type of such SPP resonances, which are excited al lower wavelengths (at $\lambda=257$ nm in Fig. 3), is the SPP-induced field enhancement at the FF. Thus, as can be seen in Fig. 3, at the wavelengths corresponding to these resonances the amplitude of the field at the FF is enhanced near the surface of the cylinder and, as a consequence, the induced nonlinear effects are also stronger. On the other hand, the SPP resonances at longer wavelengths (at $\lambda=480$ nm in Fig. 3), are due to the excitation of SPPs at the SH, with no such localized modes being excited at the FF. Inasmuch as, mathematically, the SPP resonances are given by the poles of the scattering matrix in the Eq. (20), the latter type of resonances should occur when the operating wavelength is about twice as large as the wavelength at which the former type of resonances occur. This conclusion fully agrees with the results presented in Fig. 3. This distinction between the two types of SPP resonances will appear in more complex scattering geometries as well. Importantly, a further increase in the strength of the nonlinear interaction can be achieved by tuning the parameters of the cylinder, so as the two types of resonances are excited at the same wavelength. This effect has been recently observed in the case of wave scattering by dielectric cylinders.[52]

B. Linear and nonlinear wave scattering by a metallic dimer

The wave scattering by a metallic nanodimer, which we analyze in this section, has a series of important technological applications that rely on the enhancement of the electric field at the surface of metals. Specifically, by using metallic nanodimers one can generate large electric fields, especially in the space between the metallic cylinders forming the dimer. As a result, because nonlinear optical effects at metal/dielectric interfaces, such as SHG and SERS, are strongly dependent on the physical properties of the interface, metallic nanodimers can be used efficiently in sensing applications or surface optical microscopy. Importantly, in the linear case there is an analytical solution to the problem of wave scattering by two cylinders;[53] however, in the nonlinear case no analytic solution is known yet. Therefore, numerical simulations play an important role in understanding the nonlinear wave scattering by these and other more complex nanostructures.

In our analysis, we have considered a dimer consisting of two cylinders with radius $R=200$ nm, separated by a distance d. The results of our numerical study are summarized in Figs. 4 and 5, which correspond to the separation distance $d=20$ nm and $d=100$ nm, respectively. The dispersion plots presented in these figures show that, similar to the case of a single cylinder, the scattering cross section of a metallic dimer presents a series of spectral peaks (SPP bands), at both the FF and the SH. These bands are located in the same spectral regions as in the case of a single cylinder, although the wavelength of the peaks is slightly blue shifted. This shift in the frequency of the SPP resonances is induced by the interaction between the SPPs excited on each cylinder, a physical effect that resembles the hybridization of atomic orbitals. As expected, this blue shift in the wavelength of the SPP resonances decreases as the separation distance d increases. The strength of the coupling between the SPP modes of single cylinders is also illustrated by the field profiles presented in panels D in Figs. 4 and 5. Thus, these field profiles are almost independent on the angle of incidence ϕ_0 (the angle made by the incident wave with the longitudinal axis of the dimer), which proves that this field is chiefly the result of near field interactions. This same strong SPP coupling explains the fact that the spectral location of the SPP bands in Figs. 4 and 5 does not depend on the angle ϕ_0. On the other hand, the scattering cross sections at both the FF and SH increase with the angle ϕ_0, which is due to a more efficient coupling between the incident wave and the dimer at larger ϕ_0. Furthermore, similar to the case of a single

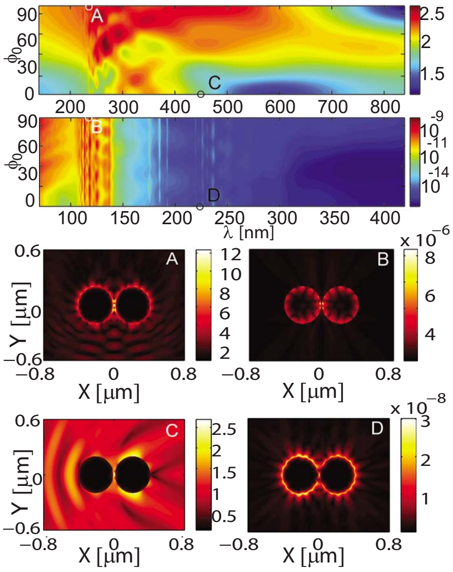

FIG. 4. (Color online) The top two panels present the scattering cross section at the FF (upper panel) and the SH (lower panel) vs. the angle of incidence and wavelength. The radius of the cylinders is $R=200$ nm and the separation distance is $d=20$ nm. The spatial profile of the amplitude of the electric field, calculated at $\lambda=237$ nm and $\phi_0=90°$ (A and B) and $\lambda=473$ nm and $\phi_0=0°$ (C and D), are plotted in the bottom panels. Left and right panels correspond to the FF and SH, respectively.

cylinder, the SPP resonances at the SH can be divided into two types, those induced by the resonant excitation of SPP modes at the FF and those that are associated with the excitation of SPP modes solely at the SH.

Additional physical insights into the properties of the wave scattering by a metallic dimer are revealed by the differential scattering cross sections presented in Figs. 6 and 7, the plots in these figures corresponding to a separation distance of $d=20$ nm and $d=100$ nm, respectively. As expected, when the direction of the incoming wave vector coincides with one of the symmetry axes of the dimer, the spatial pattern of the far-field response is also symmetric with respect to this axis; however, at an oblique angle of incidence the scattering pattern is no longer symmetric. In addition, the angular dependence of the differential scattering cross section shows that at the FF most of the scattered field is emitted in the forward direction. On the other hand, because of the intricate distribution of the sources of the SH (the surface and bulk nonlinear polarizations), the scattering pattern of $q_s(\varphi;\Omega)$ presents a much more complex dependence on the polar coordinate φ. Moreover, since the distribution of the sources of the SH depends strongly on the separation distance between the cylinders, the scattering pattern at the SH also changes significantly with this distance (see Figs. 6 and 7).

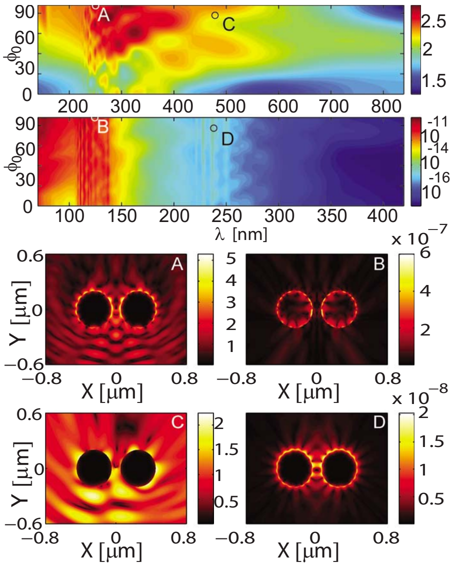

FIG. 5. (Color online) The same as in Fig. 4, but for $d=100$ nm. The field profiles correspond to $\lambda=243$ nm and $\phi_0=90°$ (A and B) and $\lambda=475$ nm and $\phi_0=78°$ (C and D).

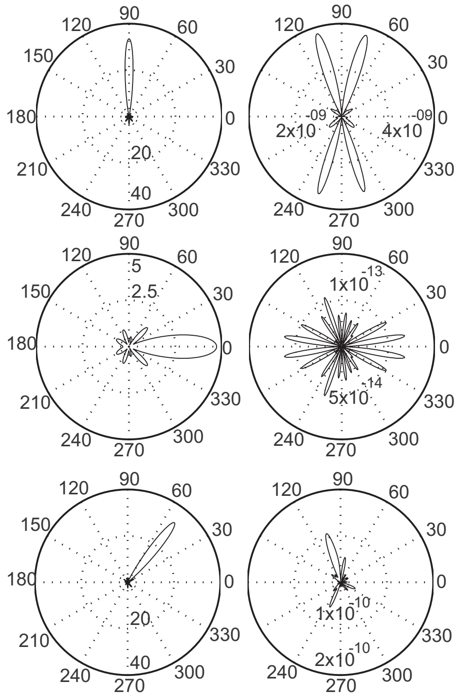

FIG. 6. Polar representation of the differential scattering cross section for a metallic dimer with $R=200$ nm and $d=20$ nm. The plots correspond to $\lambda=237$ nm and $\phi_0=90°$ (upper panels); $\lambda=437$ nm and $\phi_0=0°$ (middle panels); and $\lambda=266$ nm and $\phi_0=62°$ (bottom panels). Left and right panels correspond to the FF and SH, respectively.

The spectral characteristics of the scattering cross sections provide us with insightful information about the transfer of energy from the incident wave to the far-field. In turn, the spectra of the absorption cross sections reveal important properties of the fundamental and harmonic near-fields. In order to illustrate this idea, we present in Fig. 8 the scattering and absorption cross sections for a metallic dimer, as well as the field profiles corresponding to certain resonance wavelengths. This figure reveals several notable dependencies between the spatial profile of the fundamental and harmonic near-fields and the spectra of the scattering and absorption cross sections. First, at both the FF and the SH the spectral

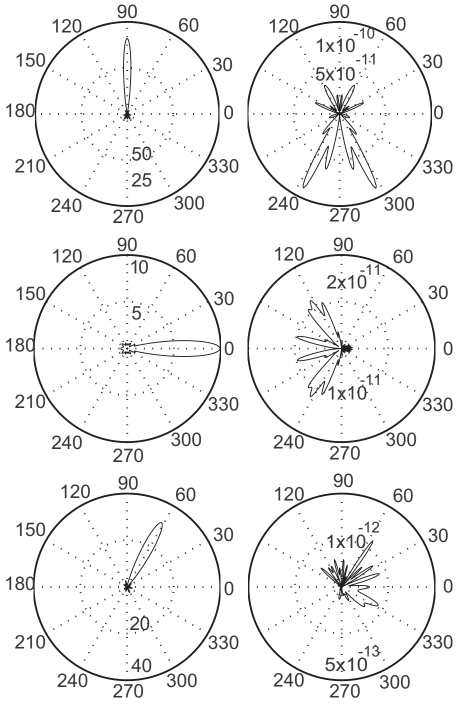

FIG. 7. The same as in Fig. 6, but for $d=100$ nm. The plots correspond to $\lambda=243$ nm and $\phi_0=90°$ (upper panels); $\lambda=232$ nm and $\phi_0=0°$ (middle panels); and $\lambda=328$ nm and $\phi_0=62°$ (bottom panels). Left and right panels correspond to the FF and SH, respectively.

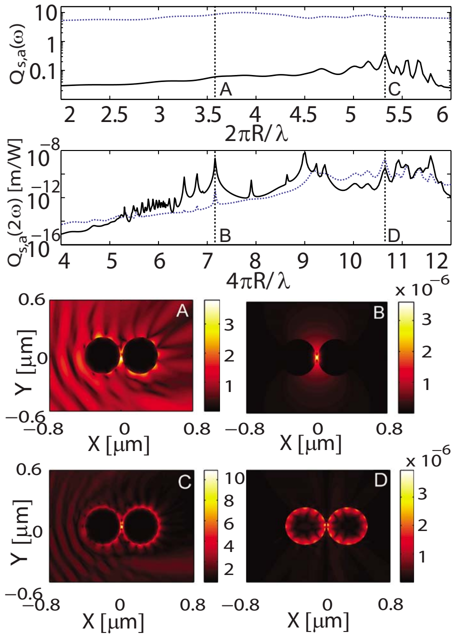

FIG. 8. (Color online) The top panels show the absorption (solid line) and scattering (dashed line) cross sections. The radius is $R=200$ nm and the separation distance $d=20$ nm. The spatial profile of the amplitude of the electric field for $\lambda=350$ nm and $\phi_0=20°$ (A and B) and $\lambda=236$ nm and $\phi_0=20°$ (C and D) is presented in the bottom panels. Left and right panels correspond to the FF and SH, respectively.

resonances of the absorption and scattering cross sections do not always coincide, which proves that they have different physical origins. Moreover, the spectral peaks in the absorption cross section at the FF correspond to a significant increase in the near-field, at the wavelength of the largest peak the field being enhanced by more than an order of magnitude (compare panels A and C in Fig. 8). Furthermore, the spectral resonances seen in the SH spectrum have different origins, too. Thus, the excitation within a small spatial domain in-between the cylinders of a strong field, a so-called "hot spot," is directly related to the resonance at $\lambda=350$ nm. On the other hand, the resonance at $\lambda=236$ nm is due to the excitation of a localized mode than penetrates into the cylinders up to a considerable depth. Interestingly enough, the panels C and D in Fig. 8 show that at $\lambda=236$ nm the field at the FF penetrates into the cylinders only a very small distance while at the SH the penetration depth is considerably larger. This effect is explained by the fact that at the SH the wavelength is smaller than the plasma wavelength ($\lambda_p=139.6$ nm), and therefore at this wavelength the cylinders have dielectric properties, namely, the real part of the permittivity is positive. At the FF, however, $\lambda>\lambda_p$, which means that the permittivity has the optical properties of a metal. Finally, note that whereas at the FF the scattering cross section is more than two orders of magnitude larger than the absorption cross section, at the SH the absorption cross section is larger than the scattering cross section in almost the entire spectral domain considered in our calculations.

C. Wave scattering from 1D chains of metallic cylinders

We have applied our numerical method to study the SHG in more complex scattering geometries, namely, chains of coupled metallic cylinders. Such nanostructures can find important technological applications to subwavelength active optical waveguides, optical nanoantennae, or light focusing at subwavelength scale.

The geometry considered in our study consists of $N=12$ metallic cylinders arranged in a linear chain, the radius of the cylinders and the separation distance being $R=200$ nm and $d=20$ nm, respectively. The main results pertaining to this scattering geometry are summarized in Figs. 9 and 10, the angle of incidence corresponding to these figures being $\phi_0=0°$ and $\phi_0=90°$, respectively (ϕ_0 is the angle between the direction of the incident wave and the axis of the chain of cylinders). One of the main conclusions illustrated by these figures is that, for both angles of incidence, the complexity of the scattering spectra increases with the number of scatters. This fact suggests that as the number of scatterers increases, the long-range interactions among the scatterers becomes stronger and therefore they play an increasingly important role in determining the global optical response of the structure. This coherent response of the scatterers is illustrated by the top two panels in Fig. 9, which show that although the spectrum of the scattering cross section at the FF has a large peak at $\lambda=313$ nm, no spectral resonance exists at the SH. To be more specific, it can be seen that at this wavelength most of the SH field (and consequently the nonlinear polarization) is localized in the region in-between

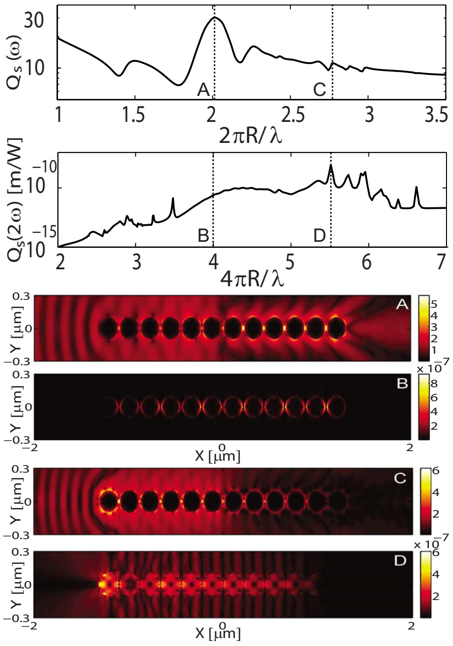

FIG. 9. (Color online) The top two panels show the spectra of the scattering cross section corresponding to a chain of $N=12$ metallic cylinders. The radius is $R=100$ nm, the angle of incidence is $\phi_0=0°$, and the separation distance is $d=20$ nm. The spatial profile of the amplitude of the electric field, calculated at $\lambda=313$ nm (A and B) and $\lambda=229$ nm (C and D), is presented in the bottom panels. The panels A and C correspond to the FF, whereas the panels B and D correspond to the SH.

adjacent cylinders (see panels A and B in Fig. 9), leading to a destructive interference in the far-field of the radiated light. As we will see in the next section, this coherent optical response of the scatterers is even more evident in the case of 2D ordered distributions of cylinders.

Figures 9 and 10 demonstrate that the wave scattering by the chain of cylinders is strongly dependent both on the wavelength as well as the angle of incidence. In particular, Fig. 9 shows that, depending on the excitation frequency, the chain of metallic cylinders supports either modes that propagate only at the FF (panels A and B) or propagating modes at both the FF and SH (panels C and D). Importantly, the latter ones can find important applications to subwavelength active nanodevices,[30] which can be used to generate and transport optical power at subwavelength scale. Another notable effect illustrated in the panel A in Fig. 9 is the formation at the end of the chain of cylinders of an optical beam with width of about $\lambda/3$, a so-called optical nanojet, an effect that can be employed to achieve subwavelength light focusing. On the other hand, one can see in Fig. 10 that, as expected, an incoming wave that is normally incident onto the axis of the chain ($\phi_0=90°$) leads to the excitation of standing waves in the chain of cylinders. Indeed, since in this case the projection of the wave vector of the incoming wave onto the longitudinal axis of the chain of cylinders cancels, no propagating modes can be excited.

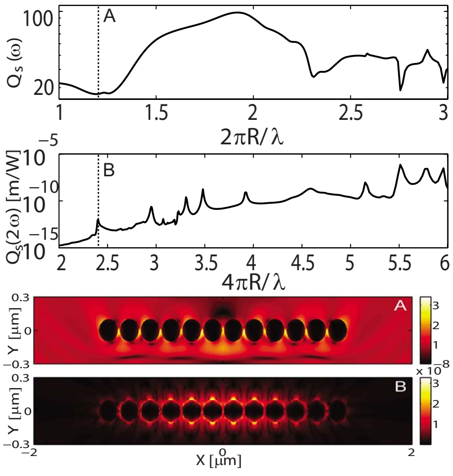

FIG. 10. (Color online) The same as in Fig. 9, but for $\phi_0=90°$ and $\lambda=525$ nm.

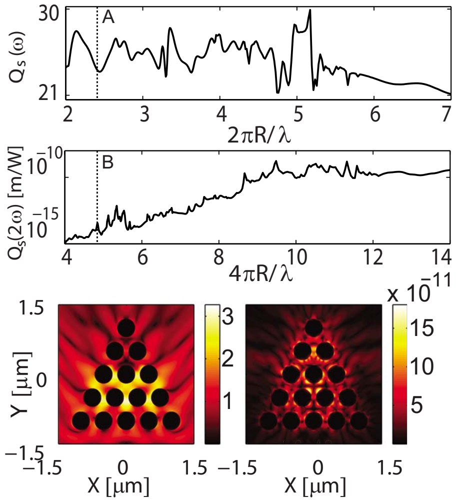

FIG. 11. (Color online) The top two panels show the spectra of the scattering cross section corresponding to a hexagonal distribution of $N=15$ metallic cylinders. The radius is $R=200$ nm, the angle of incidence is $\phi_0=90°$, and the separation distance is $d=100$ nm. The spatial profile of the amplitude of the electric field, calculated at $\lambda=471$ nm, is presented in the bottom panels. Left and right panels correspond to the FF and SH, respectively.

D. Wave scattering by ordered 2D distributions of metallic cylinders

As stated before, the versatility of the MSM algorithm allows one to study the linear and nonlinear wave scattering in cases in which the scatterers are characterized by a complex spatial distribution. As examples of such complex geometries, we consider in this Sec. II D hexagonal and square distributions of metallic cylinders. The main results regarding these scattering structures are summarized in Figs. 11 and 12 and correspond to hexagonal and square distributions, respectively. Similar to the case of 1D chains of metallic cylinders, both these geometries show a significant increase in the number of resonances in the spectrum of the scattering cross section, at both the FF and the SH. As discussed in the previous section, this effect is the result of the coherent response of the ensemble of cylinders. In addition, in the case

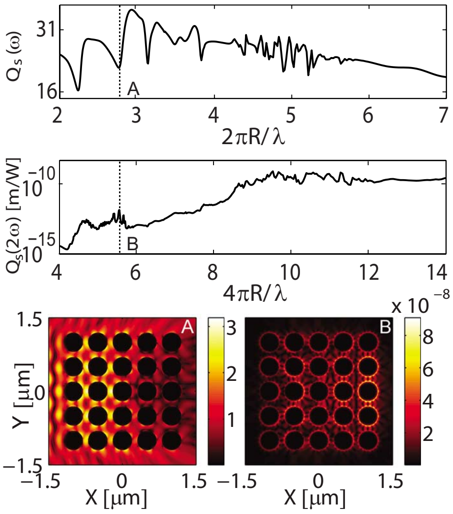

FIG. 12. (Color online) The same as in Fig. 11, but for a square distribution of $N=25$ metallic cylinders. In the bottom panels the wavelength is $\lambda=454$ nm and the angle of incidence is $\phi_0=0°$.

of 2D distributions SPPs excited on more than two cylinders can couple, leading to a more intricate interaction among these SPP modes. Moreover, note that as the wavelength decreases the scattering cross section at the SH increases. This dependence is a direct consequence of the fact that at shorter wavelengths the incident field penetrates deeper into the distribution of scatterers and therefore it induces a larger nonlinear polarization.

As can be seen in Figs. 11 and 12, the spatial field distribution inside the ensemble of cylinders changes significantly with the layout of the scatterers, a property that can be used to tune the linear and nonlinear optical response of metamaterials based on such primary building blocks. Alternative potential technological applications are suggested by the field profiles in Fig. 11. Thus, as can be seen in this figure, the hexagonal distribution of cylinders concentrates the incident field toward the tip of the set of scatterers, especially at the SH. Therefore, such a scattering geometry can be used to efficiently focus and couple the optical near-field in guiding nanostructures, such as the chain of nanowires studied in the preceding section. Interestingly enough, Fig. 12 shows that in the case of the square distribution of cylinders the field generated at the SH is stronger at the back side of the ensemble of scatterers. This surprising result can be explained by the fact that at the front side of the ensemble of cylinders the phase of the electric field is rather uniform along a plane that is parallel to the first row of cylinders, whereas deeper into the distribution of cylinders the spatial profile of the phase of the electric field becomes strongly inhomogeneous. As a result, the nonlinear polarization induced on the surface of adjacent cylinders at the front side of the ensemble of cylinders would cancel and therefore the amplitude of the generated field at the SH is small. As the field at the FF penetrates further into the distribution of cylinders it becomes strongly inhomogeneous and therefore a considerably larger amount of surface nonlinear polarization is generated.

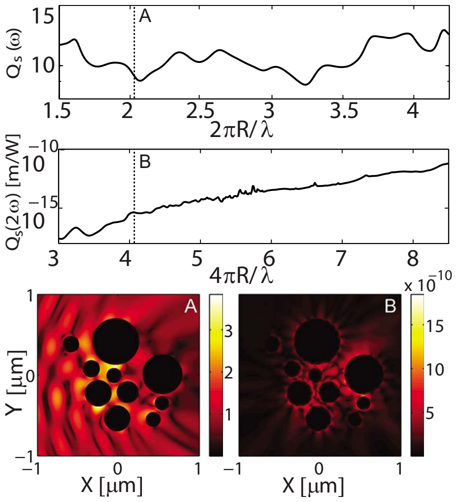

FIG. 13. (Color online) The top two panels show the spectra of the scattering cross section corresponding to a random distribution of metallic cylinders. The spatial profile of the amplitude of the electric field, calculated at $\lambda=600$ nm and $\phi_0=0°$, is presented in the bottom panels. Left and right panels correspond to the FF and SH, respectively.

E. Second harmonic generation in 2D random distributions of metallic cylinders

The last geometry we investigate is that of a 2D random distribution of metallic cylinders. In this case, both the location of the cylinders as well as their radius are random variables, the only imposed constraint being that the cylinders do not overlap. The results corresponding to one such random ensemble of cylinders are presented in Fig. 13. It can be seen in this figure that, as in the case of ordered distributions of cylinders, the scattering cross section at the SH increases as the wavelength decreases. Again, this effect is explained by a stronger nonlinear interaction at shorter wavelengths. In addition, the scattering spectra show fewer spectral features as compared to those corresponding to ordered distributions of cylinders, which is a direct consequence of the inhomogenous spectral broadening of the scattering resonances corresponding to single cylinders. It can, in fact, be argued that most of the spectral peaks seen in Fig. 13 are due to resonances associated to individual cylinders (or cylinders of similar size), the coherent contribution to the scattering spectra being smaller in this case as compared to the case of ordered distributions. Nonetheless, the interaction among the cylinders is evident in this case, too, leading to a field enhancement in the spaces between the cylinders (cavity effect) at both the FF and SH. Even if such structures do not show the intricate scattering patterns seen in our previous examples, they can nonetheless prove important for applications such as light localization. However, further studies of these effects would require a much larger number of scatterers.

V. CONCLUSION

To conclude, we have introduced in this paper a formalism, based on the MSM method, for studying the linear and nonlinear scattering effects in a metamaterial made of centrosymmetric nanowires. In our approach we have considered both the surface and bulk contributions to the nonlinear polarization. We have also shown how a series of physical quantities, such as the total cross section, the scattering cross section, the absorption cross section, and the differential scattering cross section, can be calculated and used to characterize the wave scattering process. The MSM formalism we have introduced proves to be a robust and powerful method for analyzing the linear and nonlinear wave scattering, while at the same time providing a high degree of versatility in choosing the scattering geometries that can be investigated. The numerical method has been used to study the properties of the electromagnetic field generated by the wave scattering by distributions of metallic cylinders, at both the FF and SH. One of the main conclusions of our study is that the linear and nonlinear optical response of all ensembles of metallic cylinders considered in our work is strongly influenced by the excitation of SPP resonances. The physical origin of these SPP resonances has also been elucidated and discussed.

The relation between the geometry and spatial distribution of the scatterers, on one hand, and, on the other hand, the overall response of the ensemble of metallic cylinders has also been analyzed. We have demonstrated that small variations in either the shape of the primary scatterers or the intrinsic structure (spatial distribution) of the ensemble of scatterers can lead to significant changes in both the far-field optical response as well as in the spatial profile of the near-field, at both the FF and SH. It has been revealed that this dependency of the optical response of the ensemble of scatterers on its material and geometrical parameters is especially enhanced when SPPs are excited. A complete characterization of this relationship would represent an important step forward toward developing a comprehensive theoretical description of the effective nonlinear optical properties of metamaterials. Several potential technological applications of the scattering geometries considered in this work have also been discussed. Finally, it should be noted that the results reported in this work apply not only to metallic cylinders but also to other deeply scaled down nanostructures whose optical properties are similar to those of metals, such as metallic carbon nanotubes.[54,55]

ACKNOWLEDGMENTS

We are grateful to A. Fernandez for many useful discussions. The authors acknowledge the use of the UCL Legion High Performance Computing Facility, and associated support services, in the completion of this work. This work was supported by the UK Engineering and Physical Sciences Research Council (EPSRC), under Grant No. EP/G030502/1.

---

[*] c.biris@ee.ucl.ac.uk

[1] J. B. Pendry, A. J. Holden, D. J. Robbins, and W. J. Stewart, IEEE Trans. Microwave Theory Tech. **47**, 2075 (1999).

[2] S. Linden, C. Enkrich, M. Wegener, J. Zhou, T. Koschny, and C. M. Soukoulis, Science **306**, 1351 (2004).

[3] S. Zhang, W. Fan, B. K. Minhas, A. Frauenglass, K. J. Malloy, and S. R. J. Brueck, Phys. Rev. Lett. **94**, 037402 (2005).

[4] W. Cai, U. K. Chettiar, H. K. Yuan, V. C. de Silva, A. V. Kildishev, V. P. Drachev, and V. M. Shalaev, Opt. Express **15**, 3333 (2007).

[5] R. A. Shelby, D. R. Smith, and S. Schultz, Science **292**, 77 (2001).

[6] N. C. Panoiu and R. M. Osgood, Phys. Rev. E **68**, 016611 (2003); Opt. Commun. **223**, 331 (2003).

[7] S. Zhang, W. Fan, N. C. Panoiu, K. J. Malloy, R. M. Osgood, and S. R. J. Brueck, Phys. Rev. Lett. **95**, 137404 (2005).

[8] V. M. Shalaev, W. Cai, U. K. Chettiar, H.-K. Yuan, A. K. Sarychev, V. P. Drachev, and A. V. Kildishev, Opt. Lett. **30**, 3356 (2005).

[9] N. Liu, H. Guo, L. Fu, S. Kaiser, H. Schweizer, and H. Giessen, Nat. Mater. **7**, 31 (2008).

[10] G. V. Eleftheriades, A. K. Iyer, and P. C. Kremer, IEEE Trans. Microwave Theory Tech. **50**, 2702 (2002).

[11] C. Caloz, A. Sanada, and T. Itoh, IEEE Trans. Microwave Theory Tech. **52**, 980 (2004).

[12] D. Sievenpiper, L. Zhang, R. F. J. Broas, N. G. Alexopolous, and E. Yablonovitch, IEEE Trans. Microwave Theory Tech. **47**, 2059 (1999).

[13] A. Alù and N. Engheta, Phys. Rev. E **72**, 016623 (2005).

[14] U. Leonhardt, Science **312**, 1777 (2006).

[15] J. B. Pendry, D. Schurig, and D. R. Smith, Science **312**, 1780 (2006).

[16] J. Li, L. Zhou, C. T. Chan, and P. Sheng, Phys. Rev. Lett. **90**, 083901 (2003).

[17] R. W. Ziolkowski, Phys. Rev. E **70**, 046608 (2004).

[18] N. C. Panoiu, R. M. Osgood, S. Zhang, and S. R. J. Brueck, J. Opt. Soc. Am. B **23**, 506 (2006).

[19] S. Kocaman, R. Chatterjee, N. C. Panoiu, J. F. McMillan, M. B. Yu, R. M. Osgood, D. L. Kwong, and C. W. Wong, Phys. Rev. Lett. **102**, 203905 (2009).

[20] R. M. Roth, N. C. Panoiu, M. M. Adams, J. I. Dadap, and R. M. Osgood, Opt. Lett. **32**, 3414 (2007).

[21] W. Fan, S. Zhang, N. C. Panoiu, A. Abdenour, S. Krishna, R. M. Osgood, K. J. Malloy, and S. R. J. Brueck, Nano Lett. **6**, 1027 (2006).

[22] J. A. H. van Nieuwstadt, M. Sandtke, R. H. Harmsen, F. B. Segerink, J. C. Prangsma, S. Enoch, and L. Kuipers, Phys. Rev. Lett. **97**, 146102 (2006).

[23] L. Cao, N. C. Panoiu, and R. M. Osgood, Phys. Rev. B **75**, 205401 (2007); L. Cao, N. C. Panoiu, R. D. R. Bhat, and R. M. Osgood, *ibid.* **79**, 235416 (2009).

[24] I. I. Smolyaninov, A. V. Zayats, A. Gungor, and C. C. Davis, Phys. Rev. Lett. **88**, 187402 (2002).

[25] X. W. Wang, G. C. Schatz, and S. K. Gray, Phys. Rev. B **74**, 195439 (2006).

[26] A. V. Zayats, I. I. Smolyaninov, and A. A. Maradudin, Phys. Rep. **408**, 131 (2005).

[27] U. Kreibig and M. Vollmer, *Optical Properties of Metal Clusters*

(Springer-Verlag, Berlin, 1995).

[28] K. Kneipp, Y. Wang, H. Kneipp, L. T. Perelman, I. Itzkan, R. R. Dasari, and M. S. Feld, Phys. Rev. Lett. **78**, 1667 (1997).

[29] T. H. Taminiau, R. J. Moerland, F. B. Segerink, L. Kuipers, and N. F. van Hulst, Nano Lett. **7**, 28 (2007).

[30] N. C. Panoiu and R. M. Osgood, Nano Lett. **4**, 2427 (2004).

[31] G. Veronis and S. Fan, Appl. Phys. Lett. **87**, 131102 (2005).

[32] F. Ye, D. Mihalache, B. Hu, and N. C. Panoiu, Phys. Rev. Lett. **104**, 106802 (2010).

[33] B. Knoll and F. Keilmann, Nature (London) **399**, 134 (1999).

[34] R. M. Roth, N. C. Panoiu, M. M. Adams, R. M. Osgood, C. C. Neacsu, and M. B. Raschke, Opt. Express **14**, 2921 (2006).

[35] S. I. Bozhevolnyi, J. Beermann, and V. Coello, Phys. Rev. Lett. **90**, 197403 (2003).

[36] M. Breit, V. A. Podolskiy, S. Gresillon, G. von Plessen, J. Feldmann, J. C. Rivoal, P. Gadenne, A. K. Sarychev, and V. M. Shalaev, Phys. Rev. B **64**, 125106 (2001).

[37] C. Anceau, S. Brasselet, J. Zyss, and P. Gadenne, Opt. Lett. **28**, 713 (2003).

[38] J. I. Dadap, J. Shan, K. B. Eisenthal, and T. F. Heinz, Phys. Rev. Lett. **83**, 4045 (1999).

[39] J. I. Dadap, Phys. Rev. B **78**, 205322 (2008).

[40] C. I. Valencia, E. R. Mendez, and B. S. Mendoza, J. Opt. Soc. Am. B **21**, 36 (2004).

[41] E. Centeno and D. Felbacq, J. Opt. Soc. Am. B **23**, 2257 (2006).

[42] E. Centeno and D. Felbacq, J. Opt. Soc. Am. B **17**, 320 (2000).

[43] D. Felbacq, G. Tayeb, and D. Maystre, J. Opt. Soc. Am. B **11**, 2526 (1994).

[44] M. A. Ordal, R. J. Bell, R. W. Alexander, L. L. Long, and M. R. Querry, Appl. Opt. **24**, 4493 (1985).

[45] M. Abramovitz and I. Stegun, *Handbook of Mathematical Functions* (Dover, New York, 1972).

[46] J. M. Jin, *The Finite Element Method in Electromagnetics* (John Wiley & Sons, New York, 2002).

[47] T. F. Heinz, in *Nonlinear Surface Electromagnetic Phenomena*, edited by H. E. Ponath and G. I. Stegeman (Elsevier, Amsterdam, 1991), p. 353.

[48] D. Krause, C. W. Teplin, and C. T. Rogers, J. Appl. Phys. **96**, 3626 (2004).

[49] N. Bloembergen, R. K. Chang, S. S. Jha, and C. H. Lee, Phys. Rev. **174**, 813 (1968).

[50] J. D. Jackson, *Classical Electrodynamics*, 3rd ed. (John Wiley & Sons, Hoboken, 1999).

[51] V. Kuzmiak, A. A. Maradudin, and F. Pincemin, Phys. Rev. B **50**, 16835 (1994).

[52] D. C. Marinica, A. G. Borisov, and S. V. Shabanov, Phys. Rev. B **76**, 085311 (2007).

[53] H. A. Yousif and S. Kohler, J. Opt. Soc. Am. B **5**, 1085 (1988).

[54] G. Ya. Slepyan, S. A. Maksimenko, A. Lakhtakia, O. Yevtushenko, and A. V. Gusakov, Phys. Rev. B **60**, 17136 (1999).

[55] M. Y. Sfeir, F. Wang, L. Huang, C. C. Chuang, J. Hone, S. P. O'Brien, T. F. Heinz, and L. E. Brus, Science **306**, 1540 (2004).